

BSc Thesis Applied Mathematics &
Technische Natuurkunde

Axial characteristics of a focused-ultrasound-transducer array

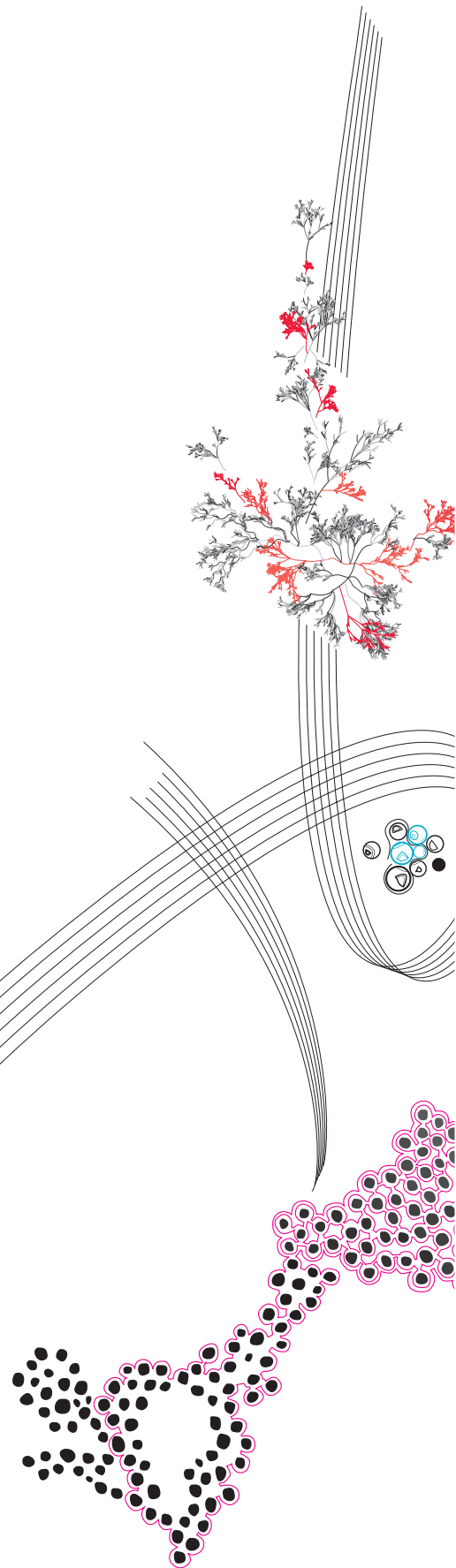
Hans-Jan Westerhof

Supervisor: Prof. dr. ir. B. J. Geurts (chair AM)
Prof. dr. ir. W. Steenberg (chair TN)
MSc. H. N. Nguyen (daily supervisor)
Prof. dr. R. J. Boucherie (external AM)
Dr. C. Blum (external TN)

June, 2019

Department of Applied Mathematics
Faculty of Electrical Engineering,
Mathematics and Computer Science

Department of Technische Natuurkunde
Faculty of Technische Natuurwetenschappen



Preface

For the past ten weeks I have been working on my bachelor's assignment with great pleasure and therefore I want to thank a number of people who helped me in the process.

First of all I want to thank Ho Nhu'Y Nguyen for being my daily supervisor. He assisted me through all the facets of the project.

Bernard Geurts and Wiendelt Steenbergen for their guidance and ideas about my research.

Richard Boucherie and Christian Blum for being the external members of my bachelor committees and for taking the time to read this thesis.

Kars Veldkamp for reading my thesis and giving fruitful feedback.

Last, but not least, I want to thank everybody from the BMPI group for the fun times during the coffee and lunch breaks.

Axial characteristics of a focused-ultrasound-transducer array

Hans-Jan Westerhof*

June, 2019

Abstract

Out-of-plane artefacts in photoacoustic imaging are a major problem and correcting the photoacoustic images is challenging. When these out-of-plane artefacts appear at the same position with in-plane features interference occurs, creating an incorrect image. Thus, correcting the image is important before interpreting the image. In this work a mathematical model describing the axial characteristics of a focused-ultrasound-transducer array is presented. The model is compared to experimentally acquired data, showing promising results.

Keywords: Photoacoustic imaging, Focused-ultrasound-transducer array, Acoustic lens

1 Introduction

The photoacoustic effect has been discovered by Alexander Graham Bell in 1881 [1]. The effect occurs when an object is illuminated, thus heated up. This heating makes the object expand. When the object is no longer illuminated it will shrink to the original size. If the illumination is done very shortly, the object will quickly expand and shrink. This creates a pressure (or acoustic) wave emitting from the object, often in the ultrasound (US) regime.

In recent years this photoacoustic effect has been the subject of research regarding the possibility of it being a method for medicinal imaging. The combination of the high resolution in ultrasound and the high optical contrast makes the method interesting for uses in medicine [2, 3]. Research on the photoacoustic effect is, for example, done on the usage for cancer detection [4, 5].

One of the biggest problems occurring in the production of photoacoustic images are artefacts. The two main types of artefacts are reflection artefacts and out-of-plane artefacts [6]. A method has been presented to identify and reduce the out-of-plane artefacts [7]. This method makes use of the movement of the out-of-plane artefact in the image, when the probe is axially moved. When the out-of-plane artefact is identified it could potentially be removed by erasing it from the image, but when the in-plane absorber and the out-of-plane artefact are at the same position in the image removing is difficult. The detected pressure is in this case the pressure of the in-plane absorber interfered with the out-of-plane artefact pressure, so erasing it from the image would also erase the information of the in-plane absorber. Correcting an image with overlapping out-of-plane and in-plane features requires knowledge about the detection of the in-plane absorbers pressure wave amplitude. Calculating the true pressure of the in-plane feature without interference

*Email: h.westerhof@student.utwente.nl

gives the opportunity to replace the interfered detected pressure wave amplitude with the calculated in-plane features pressure wave amplitude, and thus correct the image.

In this work a mathematical model is presented to predict the pressure wave amplitude of in-plane absorbers. The model can determine the pressure wave amplitude of an in-plane absorber at different axial distances from the probe. Such a model is necessary for correction of photoacoustic images as mentioned above.

The organisation of this paper is as follows:

- In section 2 the mathematical model and derivation is presented.
- Section 3 presents the experimental setup used to acquire the experimental data.
- Section 4 compares acquired experimental results with prediction of the model. Different settings of the will be evaluated in order of increasing accuracy.
- Section 5 will discuss reasons for errors between the model and the experimental data. Suggestions for future work are also presented here.

2 Theoretical model

In this section a mathematical model of a focused-ultrasound-transducer array is presented. An ultrasound-transducer array is an array of elements designed to detect ultrasound waves. All the elements in the array have an acoustic lens placed in front. This lens provides the system with the focal region at a certain distance from the lens. Objects that emit ultrasound waves in this focal region are detected with higher resolution than object outside the focal region. Figure 1 presents a schematic view of a focused-ultrasound-transducer array.

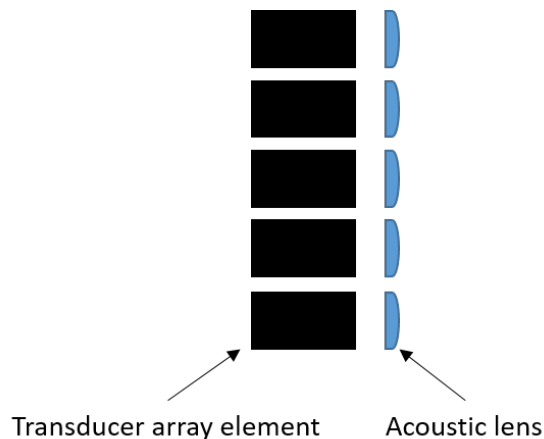


FIGURE 1: Schematic view of a focused-ultrasound-transducer array.

The model presented by Francis et al. is a nice description of a lens based acoustic imaging system [8]. In this work the type of lens differs from the lens in [8] and their model is limited to an on-axial-axis point (the axial axis is defined as the z -axis in figure 2). Where this model requires an extension that allows an off-axial-axis point source to model the entire transducer array.

The model presented here starts as a model for a single element, instead of directly for the entire array. This separation is necessary, because every array element has a lens in

front. So every array element is a lens based imaging system of its own. Meaning that every array element will react differently to the incoming acoustic wave. Eventually combining the modelled pressure at every transducer array element will give an approximation of the output from the real transducer array.

2.1 Configuration

As partially mentioned above, the model is for a system where a point source generates an acoustic wave which propagates through an acoustic lens before it is detected at a transducer array element.

Figure 2 presents a schematic overview of the system. For convenience it is placed within the (x, y) -plane, with coordinates $(x_0, y_0, 0)$. The centres of the acoustic lens and the transducer array element are on the axial axis of the space.

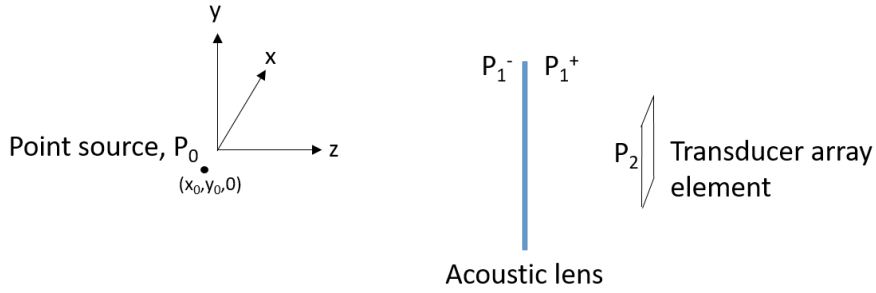


FIGURE 2: Schematic view of the lens based acoustic imaging system

2.2 Point source acoustic wave

To find the acoustic wave in the space between the point source and lens, the wave equation must be solved. The method used is via the Green's function. This method states that a partial differential equation, such as the wave equation, can be solved by convolving the source function with the impulse response, also called Green's function [9]. This is

$$\nabla^2 P_1(r, t) - \frac{1}{c_s^2} \frac{\partial^2}{\partial t^2} P_1(r, t) = P_0(r, t) \rightarrow P_1(r, t) = P_0(r, t) * p(r, t), \quad (1)$$

where $P_0(r, t)$ is the source function and $p(r, t)$ the impulse response. The source function of an ultrasound point source located at $(x_0, y_0, 0)$ having an envelop signal $a(t)$ and has as modulation wave $e^{-i\omega_0 t}$ can be defined as [8],

$$P_0(x, y, z, t) = \delta(x - x_0, y - y_0, z) a(t) e^{-i\omega_0 t}, \quad (2)$$

here $\omega_0 = 2\pi f_0$ is the angular modulation frequency corresponding to the modulation frequency f_0 . The impulse response can be found by calculating the Green's function and is given to be,

$$p(r, t) = \frac{1}{r} \delta\left(t - \frac{r}{c_s}\right). \quad (3)$$

where $r = \sqrt{x^2 + y^2 + z^2}$ and c_s is the speed of sound of the medium. As mentioned before, the acoustic wave between the point source and the lens is found by convolving the source function (2) and the impulse response (3). Performing this convolution gives

$$\begin{aligned} P_1(r, t) &= P_0(r, t) * p(r, t) \\ &= \frac{1}{r} a\left(t - \frac{r}{c_s}\right) e^{-i\omega_0\left(t - \frac{r}{c_s}\right)}, \end{aligned} \quad (4)$$

where $r = \sqrt{(x - x_0)^2 + (y - y_0)^2 + z^2}$ due to the convolution. To create the expression at the surface of the lens, the Fresnel approximation is applied to the equation for r . This gives the following $r = z + \frac{1}{2z}((x - x_0)^2 + (y - y_0)^2)$ [10]. On top of the Fresnel approximation, also the position in the z direction is taken to be the distance from the point source to the lens, or $z = z_0$. Meaning the pressure wave is described at the surface of the lens, as:

$$P_1^-(x, y, z_0, t) = \frac{1}{z_0} a\left(t - \frac{z_0}{c_s}\right) e^{-i\omega_0 t} e^{ik_0\left(z_0 + \frac{1}{2z_0}((x - x_0)^2 + (y - y_0)^2)\right)}, \quad (5)$$

Equation (5) is the expression of the acoustic wave on the surface of the lens. To this expression the effect of the lens can be added.

2.3 Wave propagation through a lens

The photoacoustic wave will pass through a plano-convex lens before it can reach the transducer array. Lenses cause a phase shift to the wave. This is applied by multiplying the incoming wave-function with the phase shift function $\Phi(x, y)$.

2.3.1 Phase shift introduced by a plano-convex lens

To derive the phase shift caused by the plano-convex lens, it is necessary to know the distance a wave will travel through the lens at different positions on the lens. Since the phase shift occurs due to the difference in distance travelled through the lens at different position on the lens. Figure 3 shows a schematic view of the lens. In this figure R is the radius of the curvature of the lens and Δ_0 is the thickness of the lens. For a circular lens, the distance a wave travels through the lens at a distance h from the centre is $\Delta_0 - \Delta_h$.

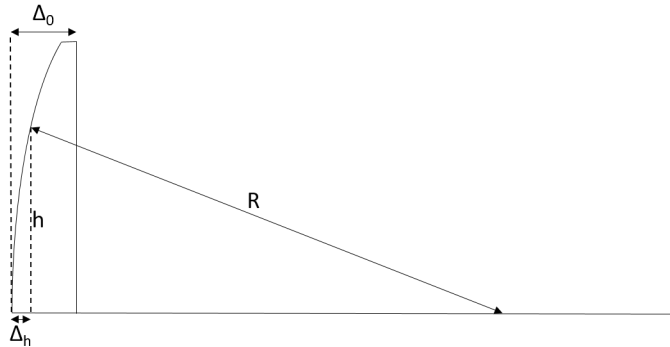


FIGURE 3: Half of a thin plano-convex lens with thickness Δ_0

The placement of the centre of the lens makes that h can be expressed by:

$$h = \sqrt{x^2 + y^2}. \quad (6)$$

From this the expression for Δ_h becomes,

$$\Delta_h = R - \sqrt{R^2 - h^2} = R - \sqrt{R^2 - x^2 - y^2}. \quad (7)$$

Because the radius of curvature is much larger than the size of the lens, $R^2 \gg x^2 + y^2$ for all x, y , it is possible to use a Taylor series expansion on the square root. Using only the first two terms gives for Δ_h ,

$$\Delta_h = R - R + \frac{x^2 + y^2}{2R} = \frac{x^2 + y^2}{2R}. \quad (8)$$

The wave travels partly through the medium surrounding the lens and partly through the lens. The wave travels a distance Δ_h through the medium surrounding the lens, and $\Delta_0 - \Delta_h$ through the lens. With the knowledge of these travelling distances, the phase shift $\Phi(x, y)$ is expressed as [10],

$$\Phi(x, y) = e^{ik_0(\Delta_h + \mu(\Delta_0 - \Delta_h))}. \quad (9)$$

Here μ is the ratio between the speed of sound in the medium around the lens and the speed of sound in the lens, $\mu = c_s/c_l$. Rewriting equation (9) and inserting the expression for Δ_h of equation (8) gives,

$$\Phi(x, y) = e^{ik_0\mu\Delta_0} e^{-ik_0\frac{x^2+y^2}{2R}(\mu-1)}. \quad (10)$$

To further explore this equation, the lensmaker's equation for thin lenses is used. The lensmaker's equation is given as [11],

$$\frac{1}{F} = (\mu - 1)\left(\frac{1}{R_1} - \frac{1}{R_2}\right), \quad (11)$$

where F, R_1, R_2 are the focal length and radii of curvature of the lens respectively. In the case of a plano-convex lens the radii are given to be $R_1 = R$ and $R_2 = \infty$. Using equation (11) in equation (10) the expression for the phase shift function is obtained.

$$\Phi(x, y) = e^{ik_0\mu\Delta_0} e^{-ik_0\frac{x^2+y^2}{2F}}. \quad (12)$$

In the case that not the entire lens is part of the system, a pupil function $\Psi(x, y)$ is introduced. This pupil function defines which part of the lens contributes to the wave after the lens.

$$\Psi(x, y) = \begin{cases} 1 & \text{if } -a \leq x \leq a, -b \leq y \leq b \\ 0 & \text{else} \end{cases} \quad (13)$$

Multiplying $P_1^-(x, y, z_0, t)$ with the phase shift function $\Phi(x, y)$ and the pupil function $\Psi(x, y)$ gives the wave just behind the lens.

$$P_1^+(x, y, z_0, t) = \Psi(x, y)\Phi(x, y)P_1^-(x, y, z_0, t) \quad (14)$$

Equation (14) defines the wave on the edge of the lens at the imaging plane side.

2.4 Wave propagation between lens and transducer array

To obtain the expression for the pressure at the transducer array element. The pressure wave on the edge of the lens is convolved with the impulse response of the medium after the lens, $P_2(x, y, z_0, t) = P_1^+(x, y, z_0, t) * h(x, y, z, t)$ [8]. Applying Fresnel approximation once more results in the following expression for the convolution [10].

$$P_2(x, y, z_0, t) = \frac{1}{z_i} \int \int P_1^+(x', y', z_0, t - \frac{z_i}{c_s}) e^{\frac{ik_0}{2z_i}((x-x')^2+(y-y')^2)} dx' dy' \quad (15)$$

Inserting equation (14) into equation (15) gives the possibility to simplify equation (15). The pupil function $\Psi(x, y)$ will give bounds to the integrals and a part of the phase shift is independent of (x, y) , thus can be taken out of the integral.

$$P_2(x, y, z_0, t) = \frac{1}{z_i} e^{ik_0\mu\Delta_0} \int_{-b}^b \int_{-a}^a e^{-ik_0 \frac{(x')^2+(y')^2}{2F}} P_1^-(x', y', z_0, t - \frac{z_i}{c_s}) e^{\frac{ik_0}{2z_i}((x-x')^2+(y-y')^2)} dx' dy' \quad (16)$$

Furthermore, the second exponent in the integral can be taken apart.

$$e^{\frac{ik_0}{2z_i}((x-x')^2+(y-y')^2)} = e^{\frac{ik_0}{2z_i}(x^2+y^2)} e^{-\frac{ik_0}{z_i}(xx'+yy')} e^{\frac{ik_0}{2z_i}((x')^2+(y')^2)} \quad (17)$$

Besides taken this exponent apart, it is possible to take $P_1^-(x', y', z_0, t - \frac{z_i}{c_s})$ apart.

$$\begin{aligned} P_1^-(x', y', z_0, t - \frac{z_i}{c_s}) &= \frac{1}{z_0} a(t - \frac{z_0}{c_s} - \frac{z_i}{c_s}) e^{-i\omega_0(t - \frac{z_i}{c_s})} e^{ik_0(z_0 + \frac{1}{2z_0}((x'-x_0)^2+(y'-y_0)^2))} \\ &= \frac{1}{z_0} a(t - \frac{(z_0 + z_i)}{c_s}) e^{-i\omega_0 t} e^{ik_0(z_0 + z_i)} e^{ik_0 \frac{1}{2z_0}((x'-x_0)^2+(y'-y_0)^2)} \end{aligned} \quad (18)$$

Inserting equation (18) into equation (16) will give the following expression,

$$P_2(x, y, z_0, t) = \frac{1}{z_0 z_i} A(t) \mathbb{P} \int_{-b}^b \int_{-a}^a e^{-ik_0 \frac{(x')^2+(y')^2}{2F}} e^{ik_0 \frac{1}{2z_0}((x'-x_0)^2+(y'-y_0)^2)} e^{\frac{ik_0}{2z_i}((x-x')^2+(y-y')^2)} dx' dy', \quad (19)$$

with

$$A(t) = a(t - \frac{(z_0 + z_i)}{c_s}) e^{-i\omega_0 t}, \quad \mathbb{P} = e^{ik_0(z_0 + z_i + \mu\Delta_0)}.$$

Inserting equation (17) into equation (19) and rearranging gives the following,

$$P_2(x, y, z_0, t) = \frac{1}{z_0 z_i} A(t) \mathbb{Q}(x, y) \mathbb{P} \int_{-b}^b \int_{-a}^a e^{-\frac{ik_0}{z_0}(x'x_0+y'y_0)} e^{-\frac{ik_0}{z_i}(x'x+y'y)} e^{\frac{ik_0}{2}L((x')^2+(y')^2)} dx' dy', \quad (20)$$

with

$$A(t) = a\left(t - \frac{(z_0 + z_i)}{c_s}\right)e^{-i\omega_0 t}, \mathbb{P} = e^{ik_0(z_0 + z_i + \mu\Delta_0)}, L = \frac{1}{z_0} + \frac{1}{z_i} - \frac{1}{F},$$

$$\mathbb{Q}(x, y) = e^{\frac{ik_0}{2z_0}(x_0^2 + y_0^2)} e^{\frac{ik_0}{2z_i}(x^2 + y^2)}.$$

The last step is removing the double integral. There are no terms where x' and y' are multiplied, so all the exponents can be split into separate exponents for the two variables. With this advantage equation (20) can be rewritten,

$$P_2(x, y, z_0, t) = \frac{1}{z_0 z_i} A(t) \mathbb{Q}(x, y) \mathbb{P} \int_{-a}^a e^{ik_0 x' \left(\frac{L}{2} x' - \frac{x_0}{z_0} - \frac{x}{z_i}\right)} dx' \int_{-b}^b e^{ik_0 y' \left(\frac{L}{2} y' - \frac{y_0}{z_0} - \frac{y}{z_i}\right)} dy'. \quad (21)$$

2.5 A better point of view

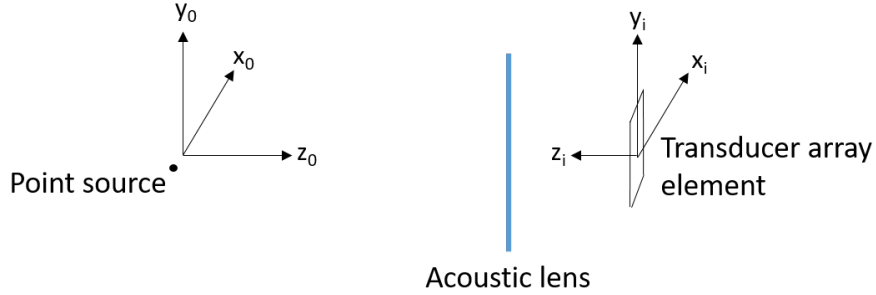


FIGURE 4: Schematic view of the system of the model

In the expression of P_2 there are still some variables in space. There are (x_0, y_0) defining the position of the point source, z_0 and z_i defining the distances from point source to lens and lens to transducer array element respectively and (x', y') to perform the convolution. For a better understanding of the model, the substitution from (x, y) to (x_i, y_i) is used. Due to the implementation of z_0 and z_i earlier, the model is bound to describe the phenomena in the plane where the transducer array element is placed. The plane in which the transducer array element is situated is called the imaging plane.

$$P_2(x_i, y_i, z_0, t) = \frac{1}{z_0 z_i} A(t) \mathbb{Q}(x_i, y_i) \mathbb{P} \int_{-a}^a e^{ik_0 x' \left(\frac{L}{2} x' - \frac{x_0}{z_0} - \frac{x_i}{z_i}\right)} dx' \int_{-b}^b e^{ik_0 y' \left(\frac{L}{2} y' - \frac{y_0}{z_0} - \frac{y_i}{z_i}\right)} dy'. \quad (22)$$

Figure 4 shows the system with the new coordinate spaces. It can be observed that the position of the point source is defined by the coordinates in the (x_0, y_0, z_0) -space, this will be called the object space. The z_0 -axis is in line with the centre of the acoustic lens and the point source is placed on the (x_0, y_0) -plane. The z_0 coordinate defines the distance from the point source to the acoustic lens. The coordinates in the (x_i, y_i, z_i) -space define the position where the pressure wave is evaluated, this space will be called the imaging space. The transducer array element is placed in the (x_i, y_i) -plane. The z_i coordinate defines the distance from the transducer array element to the acoustic lens.

All this means that the model depends on more variables than stated in equation (22). Thus, from now on the equation for the pressure at a certain position from a point source at a position will be $P_2(x_0, y_0, z_0, x_i, y_i, z_i, t)$.

Moreover, the propagation of the wave depends on wavelength. To introduce the wavelength into the equation, the relation $k_0 = \frac{2\pi}{\lambda}$ is used [12]. Inserting this into equation (22) gives,

$$P_2(x_0, y_0, z_0, x_i, y_i, z_i, t, \lambda) = \frac{1}{z_0 z_i} A(t) \mathbb{Q}(x_i, y_i) \mathbb{P} \mathbb{F}(x_0, z_0, x_i, z_i) \mathbb{G}(y_0, z_0, y_i, z_i), \quad (23)$$

with

$$\mathbb{F}(x_0, z_0, x_i, z_i) = \int_{-a}^a e^{\frac{i2\pi}{\lambda} x' (\frac{L}{2} x' - \frac{x_0}{z_0} - \frac{x_i}{z_i})} dx,$$

$$\mathbb{G}(y_0, z_0, y_i, z_i) = \int_{-b}^b e^{\frac{i2\pi}{\lambda} y' (\frac{L}{2} y' - \frac{y_0}{z_0} - \frac{y_i}{z_i})} dy'$$

Considering the objective of the model, the temporal part of equation (23) is neglected. Since only the amplitude values of the pressure in time are of interest, the interest lies solely with the non-temporal part of equation (23). Taking $P_2(x_0, y_0, z_0, x_i, y_i, z_i, t, \lambda) = A(t) P_3(x_0, y_0, z_0, x_i, y_i, z_i, \lambda)$, only $P_3(x_0, y_0, z_0, x_i, y_i, z_i, \lambda)$ will be considered from here on. Where it is

$$P_3(x_0, y_0, z_0, x_i, y_i, z_i, \lambda) = \frac{1}{z_0 z_i} \mathbb{Q}(x_i, y_i) \mathbb{P} \mathbb{F}(x_0, z_0, x_i, z_i) \mathbb{G}(y_0, z_0, y_i, z_i). \quad (24)$$

2.6 Calculating the amplitude

The expression in equation (24) can compute the amplitude of the pressure wave at a specific point in the imaging space. This is different from the detection of the amplitude in reality, where a transducer element with an area larger than an infinitesimal point detects the amplitude. To overcome this, the transducer array element is divided into a grid, seen in figure 5. At the centre of every grid rectangle P_3 is evaluated. The pressure the transducer array element detects is then the mean of the amplitude at all rectangles in the grid.

When the peak pressure of every transducer array element is calculated. It needs to be combined to obtain an output matching the output of the real transducer array. This is done by summing up all the pressures of the N elements within the transducer array. Now the peak pressure of transducer array is calculated for a point source location and could be compared with a real transducer.

3 Experimental setup

3.1 The setup

The experimental setup is shown in figure 6. It is the same setup described in [7]. A handheld US array probe has been used, which has a built-in focused-ultrasound-transducer array to detect the pressure waves. The array consists of 128 elements with a pitch of 0.245 mm. The centre frequency is 7.5 MHz with a bandwidth of 66%. This probe is connected to a commercial US scanner MyLabOne (Esaote Europe BV, The Netherlands). The scanner

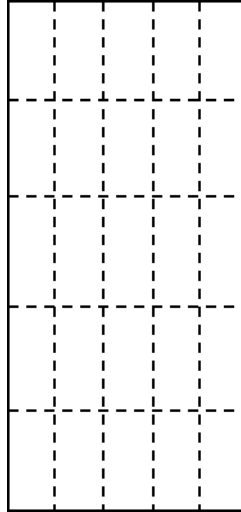


FIGURE 5: The dividing grid of a transducer array element

acquires data at a maximum sampling frequency of 50 MHz with 12 bit digitization, it was used in research mode to have access to the raw data [6].

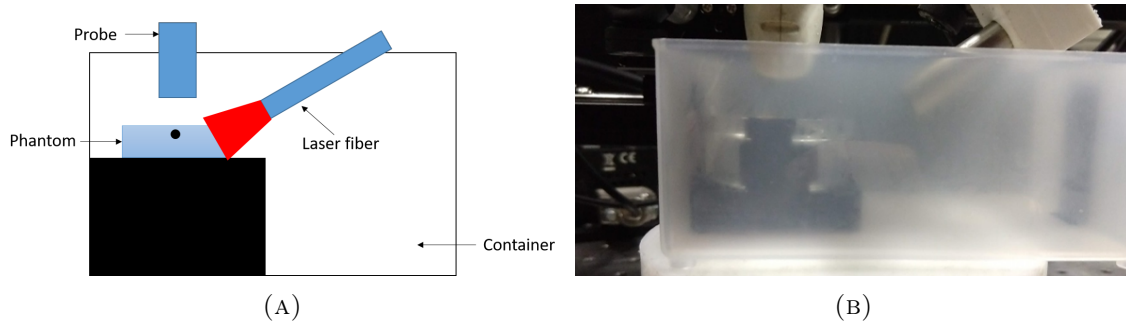


FIGURE 6: (A) Schematic figure of the experimental setup, (B) picture of the real setup

The light source is an Opolette 532 (Laser2000, The Netherlands) which emits laser light in at a tunable wavelength in the ranges (680-960 nm or 1200-1400 nm). It has a repetition rate of 20 Hz. The laser light is coupled into a multi-mode optical fiber bundle (LightGuideOptics Germany GmbH, Germany) with a core diameter of 6.5 mm [7]. To synchronize the system and trigger the laser, a function generator (AFG 3102, Tektronix, Germany) has been used. The hardware components are controlled via a LabVIEW program [7]. Figure 7 shows the setup with the movable probe and the hardware control sequency.

In the experiments laser light at a wavelength of 790 nm has been used. The pulse energy at the fiber output was 4.4 ± 0.4 mJ [7]. A phantom was made of a black absorber having a thickness of $\sim 0.1-0.15$ mm cut out from a black thread. The absorber was placed in agarose (2%) in a petri dish lid (Greiner Bio-One GmbH, Germany). The phantom is placed in a container filled with a suspension of 2% Intralipid 20% in demi-water. This emulsion is the coupling medium.

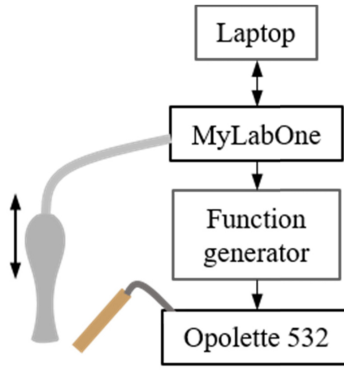


FIGURE 7: Schematic figure of the setup and control sequence [7]

3.2 Translation stage

To define the axial distance of the probe to the absorber precisely, a motorized translation stage (MTS50A-Z8, Thorlabs, Germany) is used. This stage can be controlled with LabVIEW. Controlling the stage is done most efficiently with the QMH Template of the AMC library (National Instruments, United States).

4 Results

4.1 Photoacoustic image

The first result from the experiment is a sequence of photoacoustic images. A photoacoustic image is produced with the probe at a certain distance, after the image is produced the probe moves up 0.51 mm and a second image is produced. This process is repeated until the sequence consists of 30 images. In figure 8 the first two images in the sequence are presented.

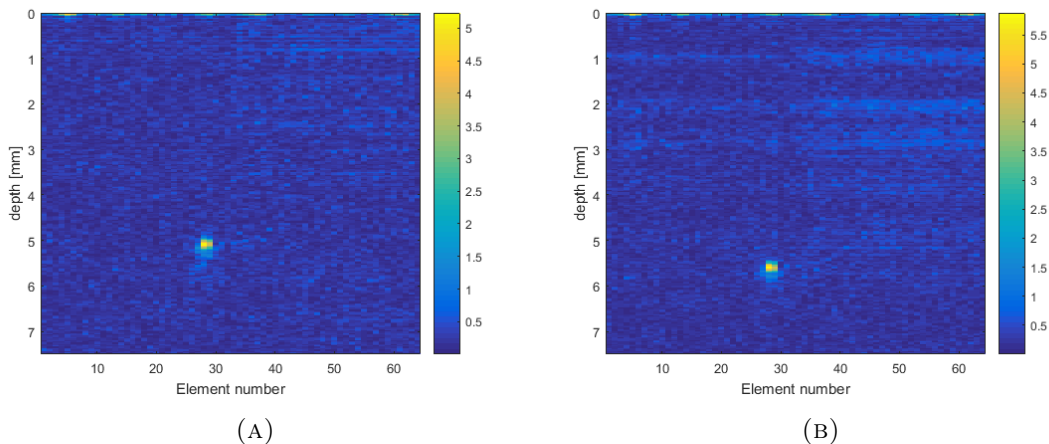


FIGURE 8: Photoacoustic images of the acquired sequence, (A) first photoacoustic image in the sequence, (B) second photoacoustic image in the sequence

In figure 8 the yellow dot is the absorber in the phantom. It can be observed from figures 8a and 8b that the absorber has moved down. It starts at a depth of ~ 5 mm in figure 8a and in figure 8b it is at a depth of ~ 5.5 mm.

For every image in the sequence the pixel value of the absorber is determined. This pixel value corresponds with the amplitude of the pressure wave. Plotting the pixel value versus the depth of the absorber gives a graph of the axial characteristics experimentally determined, shown in figure 9.

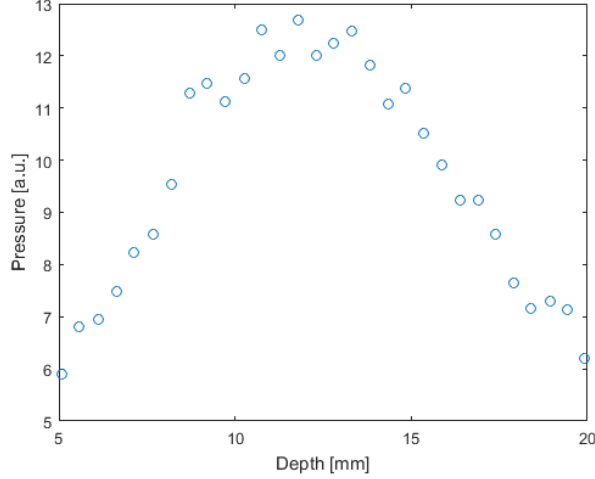


FIGURE 9: Experimentally determined axial characteristics

4.2 Calibrating the model

In order to use the model to predict the pressure at different depths and comparing it to the experimental data, the parameters in the model must be determined. Some parameters are independent on the phantom, and thus the same for every experiment. The values of these parameters can be determined before executing the experiment. The parameters and their values are determined to be:

- Speed of sound in the coupling medium, c_s , 1500 m/s
- Ration between speed of sound in lens and coupling medium, μ , 1.5
- Thickness of the lens, Δ_0 , 691 μm
- Distance between the lens and the transducer array element, z_i , 114 μm

Parameters such as the frequency of the pressure wave and the absorbers position along the transducer cannot be determined beforehand. Thus, they are taken from the experiment and put in the model to fit the experimental settings.

The frequency of the detected pressure wave is determined by performing a Fourier transform on the "raw data", which is the data before it processed into the photoacoustic image. Zero-padding has been used to increase the resolution of the frequency spectrum. The frequency spectrum of the "raw data" is shown in figure 10. The main frequency for this phantom has been determined to be 5.1 MHz.

Next, the position of the absorber along the transducer array must be determined and put into the model. This position is important, because it defines the x_0 in equation (24) for every transducer array element. The position of the absorber along the transducer array can be determined from the photoacoustic images in figure 8. From these images it can be found that the absorber is placed underneath transducer array element number 28.

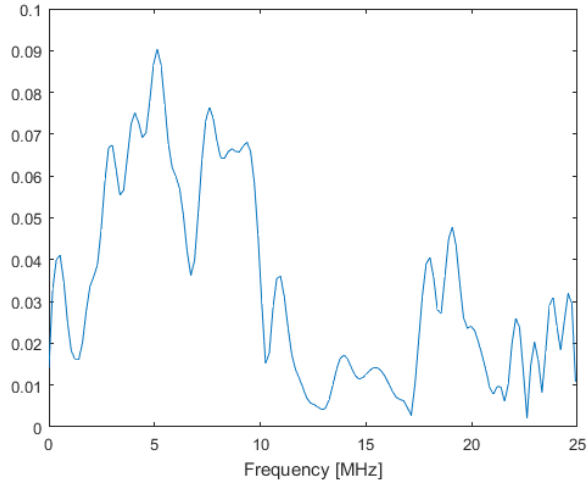


FIGURE 10: Frequency spectrum of the detected pressure wave

Finally, the depth of the maximum pressure is used as an input. This depth is z_0 in the expression for P_3 . Based on figure 9, the depth of the maximum has been determined to be at 11.8 mm for this phantom. It is necessary to know the peak depth, because the focal length of the acoustic lens is unknown. While it is known that L must be zero at the peak depth, so it is possible to calculate the focal length F by solving $\frac{1}{z_0} + \frac{1}{z_i} - \frac{1}{F} = 0$. Solving this is possible since z_0 and z_i are known.

4.3 Comparing model with experimental data

With all the parameters put into the model. The graph showing the pressure versus the depth can be calculated and compared to the experimental data. To make comparison possible, the experimental data and the modelled values are normalized. The experimental data is without units, which makes comparison of the true values not possible. Normalizing both data makes it possible to compare the shapes.

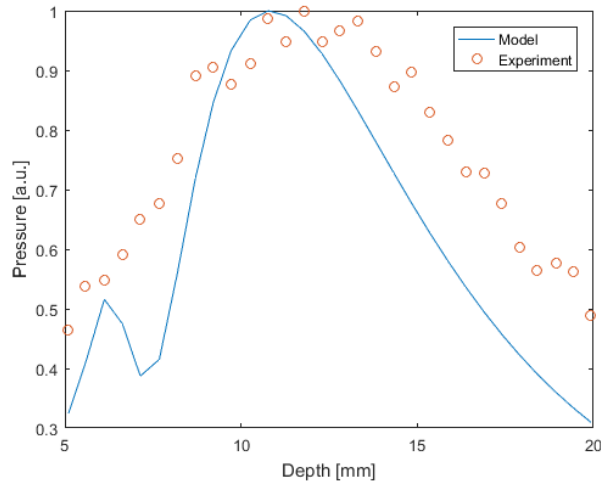


FIGURE 11: Experimental data and modelled graph

In figure 12a the experimental data and the modelled values are shown. This model

is for a frequency of 5.1 MHz, a peak depth of 11.8 mm and an absorber placed under transducer array element 28. It can be observed that the experimental data and the model do not strongly agree. The peak of the model is not at the same position as the peak of the experimental data. Also the model seems to have a narrower curve than the experimental data. The experimental data does not show any side peaks, while the model does have a side peak at approximately 6.5 mm. These differences between the model and the experimental data require improvements in the model to increase the agreement.

4.4 Multiple frequencies

The first improvement that seemed a reasonable option was to use multiple frequencies. As can be seen in figure 10 the frequency spectrum of the signal also has a peak a little to the right of the main peak. This peak is the second highest local maximum of the frequency spectrum and is placed at 7.6 MHz. This is implemented by calculating the axial characteristics for multiple frequencies and summing up these axial characteristics.

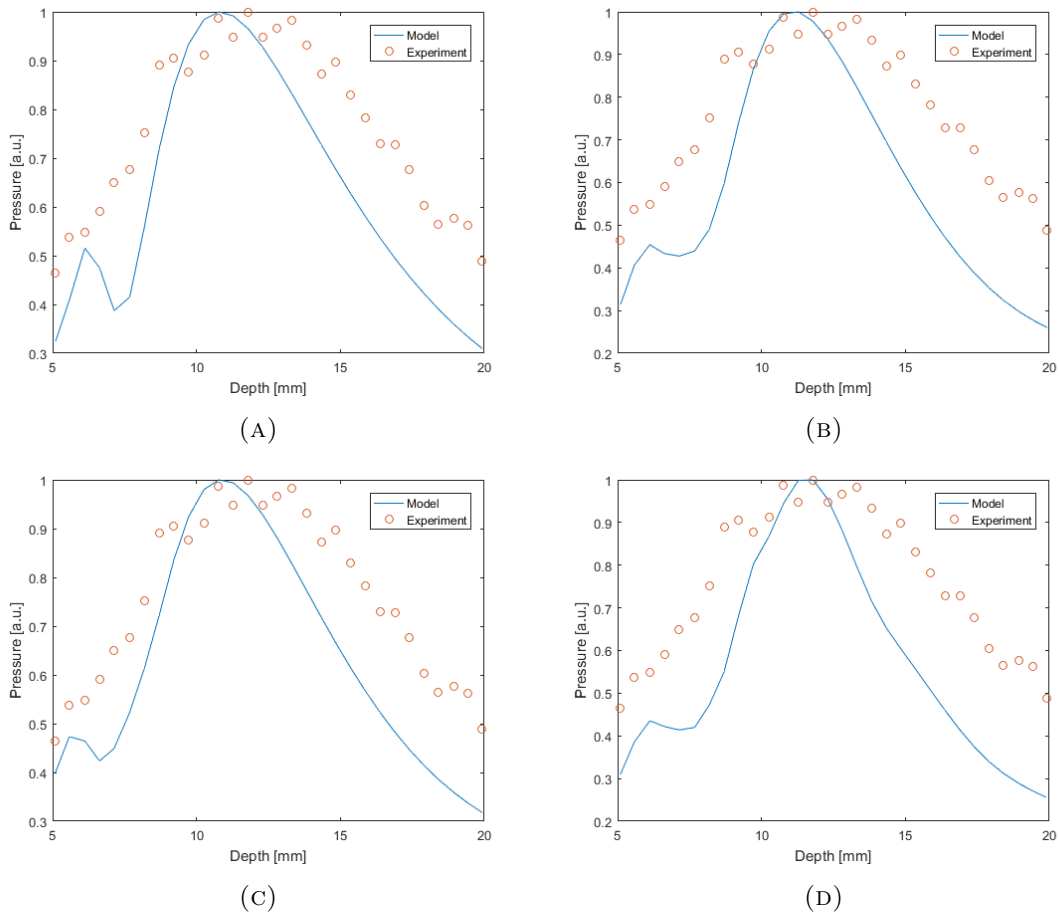


FIGURE 12: Experimental data and modelled graphs, (A) model for 5.1 MHz, (B) model for 5.1 and 7.6 MHz, (C) model for 4.0, 5.1 and 7.6 MHz, (D) model for 5.1, 7.6 and 19 MHz

Comparing figures 12a and 12b leads to the conclusion that it gives a slightly better approximation of the experimental data with multiple frequencies than only one frequency. The graph is still narrower than the experimental data, but the side peak has been reduced.

For further improvement also a third frequency is used. This is done for two different third frequencies. In figure 10 the side peak on the left of the maximum is taken as the third frequency in figure 12c, the frequency was determined to be 4.0 MHz. In figure 12d the third frequency is taken from the far right peak in the frequency spectrum, it has been determined to be 19.0 MHz.

The graphs in figure 12 show that adding a third frequency to the model barely increases in accuracy. In the case of adding the high frequency of 19 MHz the model is even worse. The modelled graph gets even sharper than in the one frequency model. Also the side peak is still present. The significant amount of increase in the computation time for increasing the amount of frequency leads to the idea that either one or two frequencies should be considered.

4.5 Different y_0 positions

Another possibility for improvement is to adjust the y_0 coordinate in the model. In the modelled values above the absorber has been placed in the (x_0, z_0) -plane, meaning that the y_0 value has been set at zero. This places the absorber in-plane, as is desired. However, it could be possible for the absorber to be just outside the in-plane in position. Figure 13 shows the orientation of the (x_0, y_0) -plane compared to the transducer array.

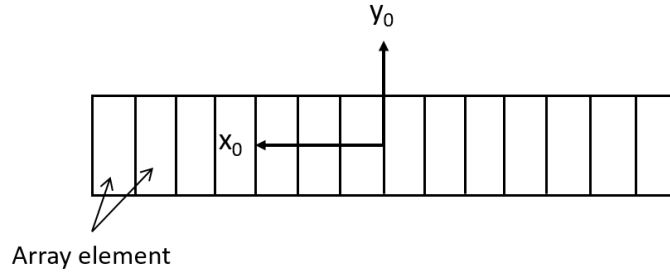


FIGURE 13: Orientation of the (x_0, y_0) -plane related to the transducer array

This is modelled by assigning a small non-zero value to y_0 . In figure 14 all the modelled graphs are done for one frequency of 5.1 MHz.

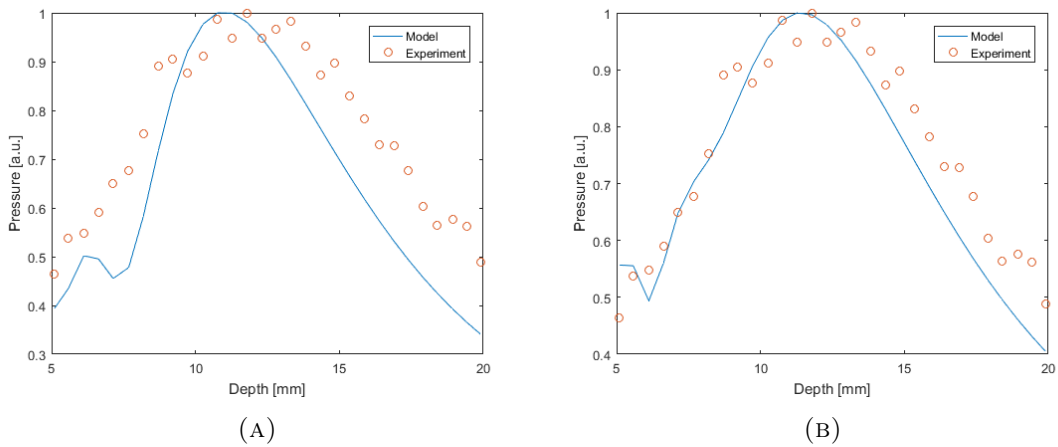


FIGURE 14: Experimental data and modelled graphs with 5.1 MHz frequency, (A) model for $y_0 = 0.1$ mm, (B) model for $y_0 = 0.2$ mm

From figure 14 it can be observed that the a value of $y_0 = 0.2$ mm gives the most accurate model of the system. The modelled graph in figure 14a shows few resemblances with the experimental data. The graph is sharper peaked and the maximum is shifted to the right. However, the modelled graph in figure 14b fits the first half of the data nicely, in the second half, it decreases more steeply than the experimental data. Furthermore, there is still a small oscillation at the start of the modelled graph for $y_0 = 0.2$ mm.

4.6 Combination of the improvements

To improve the model even further, the above two methods of improvement have been combined. The use of two frequencies and different positions of y_0 have been considered.

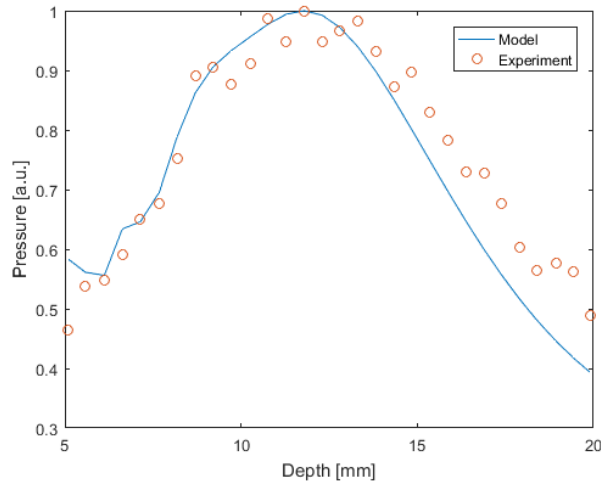


FIGURE 15: Experimental data and modelled graph with frequencies 5.1 and 7.1 MHz and $y_0 = 0.2$ mm

The best result was obtained by using the two frequencies 5.1 and 7.6 MHz and $y_0 = 0.2$ mm, seen in figure 15. It can be seen that the modelled graph is less sharp compared to the model with one frequency in figure 14b. The small oscillation is slightly reduced, although not completely removed. Compared to the data there is still room for improvement. The last 15 experimental data points show a less steep decrease compared to the modelled graph.

4.7 Other phantoms

For two more phantoms the measurements have been performed. In figure 16 is the experimental data and frequency spectrum for the second phantom presented.

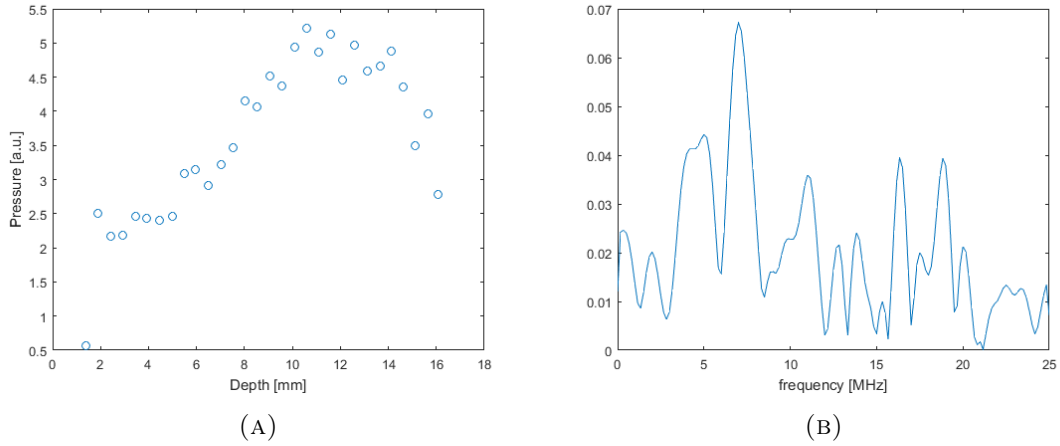


FIGURE 16: (A) Experimental data of phantom 2, (B) frequency spectrum of phantom 2

The two main frequencies for phantom 2 have been determined to be 5.0 and 7.0 MHz. In the model these two frequencies will be used. The depth at which the maximum in the experimental occurs has been determined to be 11.8 mm.

For different values of y_0 is the modelled graph calculated and the best results has been obtained for $y_0 = 0.2$ mm. This result is shown in figure 17.

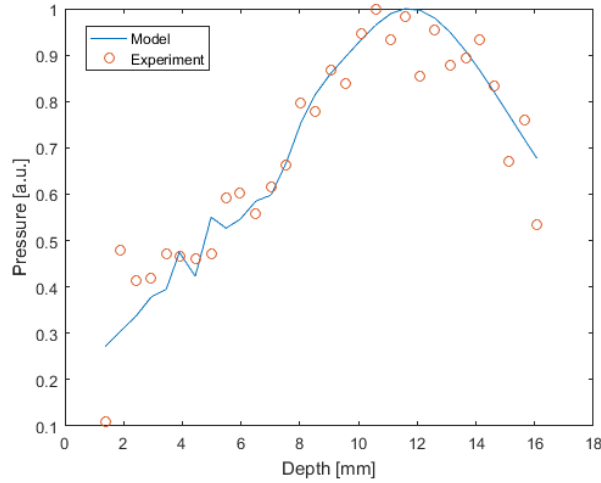


FIGURE 17: Experimental data of phantom 2 and modelled graph with frequencies 5.0 and 7.0 MHz and $y_0 = 0.2$ mm

It is quickly observed that the experimental data and the modelled graph have a great agreement. For phantom 1 the model declines more steeply than the experimental data, see figure 15, while this is not the case for phantom 2. Also there is no oscillation in this modelled graph. The modelled graph shows a few small oscillations at the small depths, but these oscillations do not influence the trend of the graph.

For a third phantom the same procedure has been followed. The experimental data and the frequency spectrum are presented in figure 18.

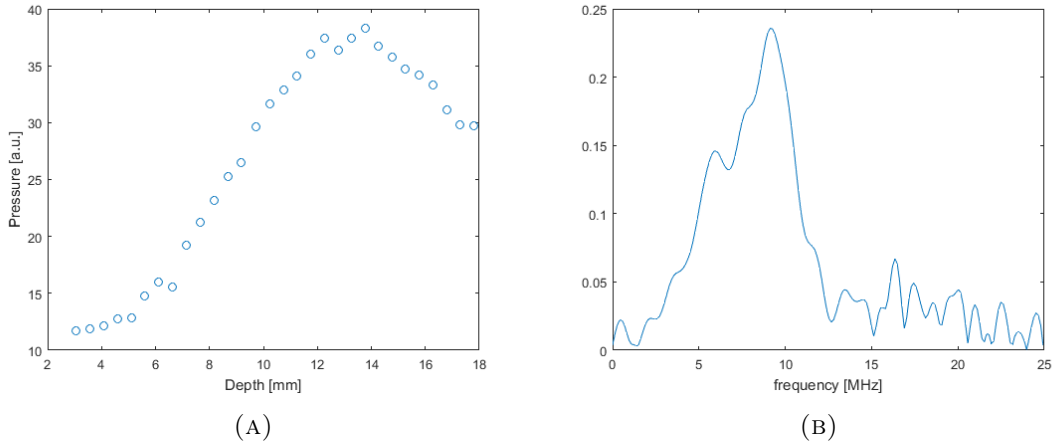


FIGURE 18: (A) Experimental data of phantom 3, (B) frequency spectrum of phantom 3

For this third phantom the used frequencies are taken to be the frequency corresponding to the maximum and the frequency corresponding to the local maximum left of the maximum, the values are 9.1 and 6.0 MHz. The maximum in the experimental data is determined to be 13.6 mm.

The value for y_0 for which the best approximation to the model was found has been determined to be 0.15 mm. The experimental data and the modelled graph are presented in figure 19.

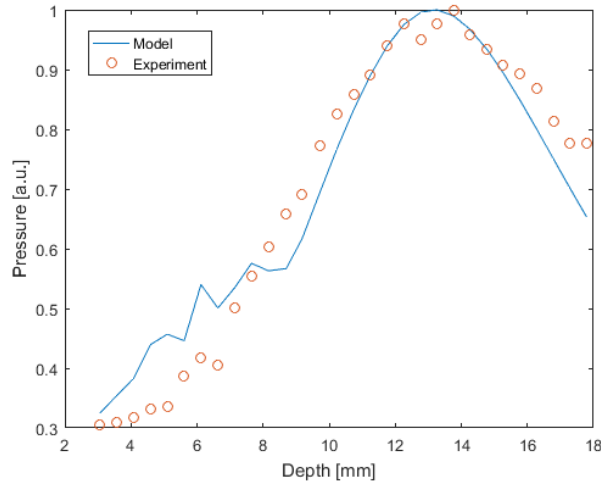


FIGURE 19: Experimental data of phantom 2 and modelled graph with frequencies 6.0 and 9.1 MHz and $y_0 = 0.15$ mm

The experimental data and the modelled graph show a small amount of agreement. The top of both curves show resemblance, but the rest of the curves do not. The modelled graph is more peaked than the experimental data. Also the modelled graph shows again these oscillations at small depths, as observed for the second phantom.

4.8 Frequency spectrum by hydrophone

To obtain more insight in the frequency spectrum of the signal, a measurement with a 0.2mm hydrophone needle (Precision Acoustics, United Kingdom) is performed. The hydrophone has a broadband frequency range (1 MHz - 35 MHz), so frequencies that are filtered out by the transducer can be made visible with the hydrophone.

The hydrophone is placed in the place of the probe in the setup of figure 6a. The hydrophone is placed at a distance of ~ 7.5 mm from the phantom. This phantom is made from a piece of black tape on a petri dish lid. Since the interest lies in the signal transmitted and not in the pressure profile there is no need to perform a sequence of measurements at different distances. A single measurement at a single distance is sufficient.

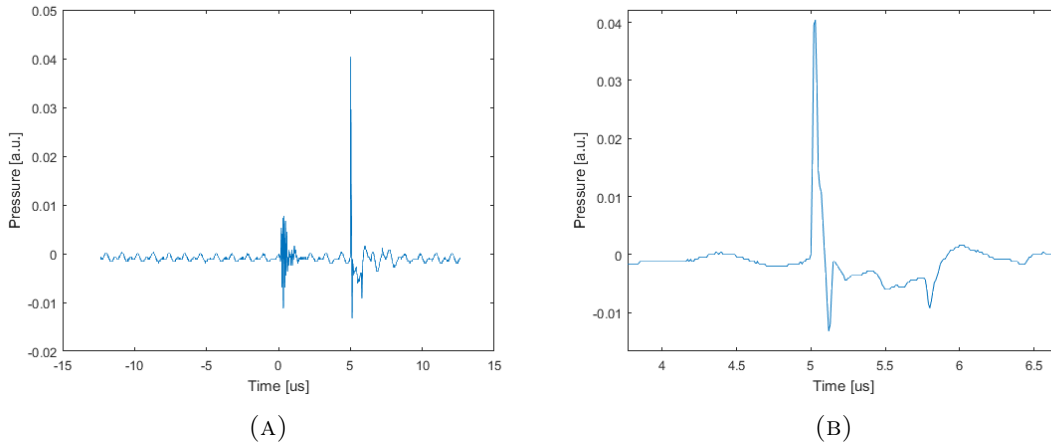


FIGURE 20: (A) Complete recorded signal with hydrophone, (B) recorded photoacoustic signal of hydrophone

In figure 20a the complete recorded signal of the signal of the hydrophone is presented. Time $0\mu\text{s}$ indicates the moment the laser light is sent out. The vibrations detected at $0\mu\text{s}$ most likely originate from the trigger signal of the laser. The sharp peak at $5\mu\text{s}$ is the photoacoustic signal from the phantom. In figure 20b a zoom-in of the photoacoustic signal is presented. The photoacoustic signal starts at $\sim 5\mu\text{s}$ and ends at $\sim 5.2\mu\text{s}$. The other possible signals in the recording are most likely reflections of the photoacoustic signal.

To obtain the frequency spectrum, the photoacoustic signal is taken out of the complete recording and zero padded. Figure 21 shows the spectrum of the signal.

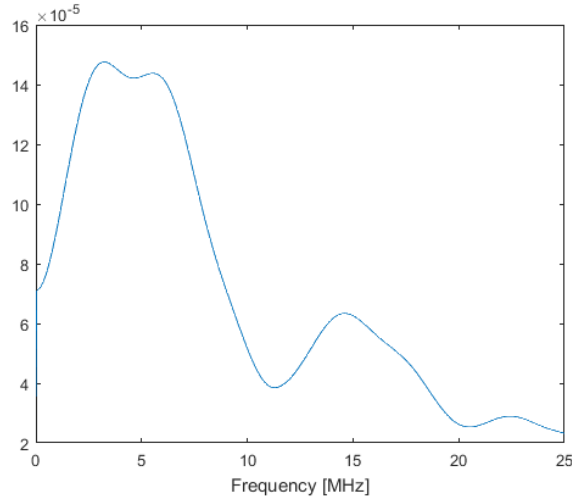


FIGURE 21: Frequency spectrum of photoacoustic signal by hydrophone

From the frequency spectrum by the hydrophone measurement can be observed that the most present frequencies are in the range of $\sim 2.5 - 6$ MHz. While the frequencies most present in the signals recorded with the probe are in the range of $\sim 5 - 10$ MHz.

Using the frequencies from the hydrophone measurement in the model, gives some interesting results. For the first phantom the usage of the frequencies from the hydrophone measurement does not show an increase in accuracy. This can be seen in figure 22. The modelled graph for the hydrophone frequencies is more peaked and shifted to the left.

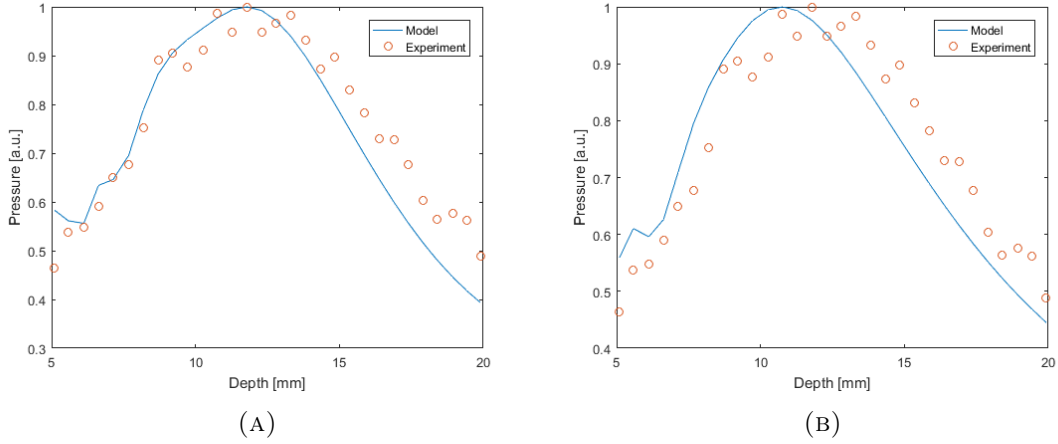


FIGURE 22: Experimental data and modelled graph with probe frequencies and hydrophone frequencies for phantom 1, (A) model with probe frequencies, (B) model with hydrophone frequencies

For the second and third phantom the accuracy also decreases if the hydrophone frequencies are used in the model. This is probably caused by the probe. Frequencies that are not close to the centre frequency of the probe are filtered out by the probe before being detected by the transducer array elements. This means that the detected signals do not contain the low frequency of 2.5 MHz that is present in the hydrophone measurement. This also explains why the model is more accurate if the probe frequencies are used, because they are in the detected signal and the hydrophone frequencies are not.

5 Discussion

5.1 Reasons for errors

Considering the results above, it can be concluded that the model shows promising results in predicting the axial pressure profile. Especially for the second phantom the experimental data and the modelled graph are in good agreement. However, for the first and third phantom there is much room for improvement. To understand the disagreement between the experimental data and modelled graphs, possible causes for errors will be discussed below.

The use of one or two discrete frequencies is most likely a cause for the observed errors. In the frequency spectra it is observable that for neither of the three phantoms one or two discrete frequencies are present in the signal, but rather a range of frequencies. Using a range of frequencies is not included in the model. The model works for a set of discrete frequencies. Besides, the model does not account for certain frequencies to be more prominently present in the signal than other frequencies. While the frequency spectra clearly show that the used frequencies have different amounts of influence on the signal.

Furthermore, the effect of the 7.5 MHz centre frequency of the probe is not part of model. It was shown that the frequencies present in the emitted signal by the absorber are not all present in the detected signal. Although not every effect caused by these frequencies is known.

The position of the absorber is also a cause for errors. The position of the absorber along the transducer array is determined by the the maximum in the photoacoustic picture. This position is then taken to be directly under a certain element. The diameter of the absorber, however, is smaller than the width of a transducer array element. Therefore, the exact position of the absorber cannot be determined and introduces a error to the model. Also the y_0 value introduces an error. At the moment different values of y_0 are tried, and the value that gives the most accurate model is chosen as the true value. This method is not the most ideal and error prone.

5.2 Suggestions for future work

Improving the model to account for the presence of frequency ranges instead of discrete frequencies would be an interesting topic for future research. The comparability of the model and reality would be increased by introducing possibility of the frequency range input.

Also the effects of the centre frequency of the probe need to become part of the model. The frequency response of the probe has not been analysed. A thorough analysis on the possible effects might lead to improvements in the model.

For further improvement, the measurement of the position of the absorber could be enhanced greatly. Designing a method to measure the position of the absorber precisely, while the probe does not need to be removed would increase modelling speed and accuracy. It would make testing different values of y_0 unnecessary and save a great amount of time.

A program that models the pressure profile semi-automatically would increase productivity. At the moment the parameters such as frequencies, pressure maximum depth and position of the absorber are modified manually. This is very time consuming. Creating a program that only requires the the sequence of photoacoustic images to compute a modelled graph automatically would help overcome these problems.

6 Conclusion

A mathematical model describing the axial characteristics of a focused-ultrasound-transducer array has been presented. Comparison between experimental data from phantoms and the model shows promising results. Although the model requires improvements to be used in the correction of photoacoustic images.

References

- [1] Alexander Graham Bell. The production of sound by radiant energy. *Science*, 2(48):242–253, 1881.
- [2] Minghua Xu and Lihong V Wang. Photoacoustic imaging in biomedicine. *Review of scientific instruments*, 77(4):041101, 2006.
- [3] Lihong V Wang and Song Hu. Photoacoustic tomography: in vivo imaging from organelles to organs. *science*, 335(6075):1458–1462, 2012.
- [4] Srivalleesha Mallidi, Geoffrey P Luke, and Stanislav Emelianov. Photoacoustic imaging in cancer detection, diagnosis, and treatment guidance. *Trends in biotechnology*, 29(5):213–221, 2011.
- [5] Michelle Heijblom, Daniele Piras, Frank M van den Engh, Margreet van der Schaaf, Joost M Klaase, Wiendelt Steenbergen, and Srirang Manohar. The state of the art in breast imaging using the twente photoacoustic mammoscope: results from 31 measurements on malignancies. *European radiology*, 26(11):3874–3887, 2016.
- [6] Ho Nhu Y Nguyen, Altaf Hussain, and Wiendelt Steenbergen. Reflection artifact identification in photoacoustic imaging using multi-wavelength excitation. *Biomedical optics express*, 9(10):4613–4630, 2018.
- [7] Ho Nhu Y Nguyen and Wiendelt Steenbergen. Reducing artifacts in photoacoustic imaging by using multi-wavelength excitation and transducer displacement. *Biomedical Optics Express*, 10(7):3124–3138, 2019.
- [8] Kalloor Joseph Francis, Bhargava Chinni, Sumohana S Channappayya, Rajalakshmi Pachamuthu, Vikram S Dogra, and Navalgund Rao. Characterization of lens based photoacoustic imaging system. *Photoacoustics*, 8:37–47, 2017.
- [9] Dean G Duffy. *Green's functions with applications*. Chapman and Hall/CRC, 2015.
- [10] Joseph W Goodman. *Introduction to Fourier optics*. Roberts and Company Publishers, 2005.
- [11] F.L. Pedrotti, L.M. Pedrotti, and L.S. Pedrotti. *Introduction to Optics: Pearson New International Edition*. Pearson Education Limited, 2013.
- [12] Glen Wade. *Acoustic imaging: cameras, microscopes, phased arrays, and holographic systems*. Plenum Press, 1976.

A MatLab code

A.1 Main code

Below is the main code used to calculate the axial pressure profile.

```
1 %% Set parameters
2 %Set physical parameters
3 frequency = [5e6 7.0e6];
4 SPEED_OF_SOUND = 1.54e3;
5 SPEED_OF_SOUND_LENS = 1e3;
6 SPEED_OF_SOUND_MATCHING = 2.179e3;
7 wavelength = SPEED_OF_SOUND./frequency;
8 wavenumber = 2*pi./wavelength;
9 wavelengthMatching = SPEED_OF_SOUND_MATCHING./frequency;
10 lensTransducerDistance = 0.114e-3;
11 peakPosition = 11.6e-3; % Dictates the depth where the peak will form
12 focalLength = ...
    (peakPosition*lensTransducerDistance)/(lensTransducerDistance+peakPosition); ...
    % Determines the focal length to fit the peak position
13 lensPointSourceDistance = ipAbsDepths.*10^(-3);
14 Δ0 = 0.691e-3; % Thickness of the lens
15 mu = SPEED_OF_SOUND/SPEED_OF_SOUND_LENS; % Ratio between sound speed ...
    outside lens and inside lens
16 pitch = 0.245e-3;
17 elevation = 5e-3;
18 a = 0.245e-3; % Size of the lens along pitch direction
19 b = 6.5e-3; % Size of the lens along elevation direction
20 centering = 23; % States under which element in the array the absorber ...
    is located
21 y0 = 1e-3; % Displacement of the absorber in the y-direction ...
    relative to the center of the array
22 totalElements = 64;
23 elementnumber = 1:totalElements;
24
25 %Create grid
26 Np = 5;
27 Ne = 5;
28 xi = -0.5*pitch + (pitch/(2*Np)): (pitch/Np): 0.5*pitch - (pitch/(2*Np));
29 yi = -0.5*elevation + ...
    elevation/(2*Ne):elevation/Ne:0.5*elevation-elevation/(2*Ne);
30
31
32 %% Calculate pressure
33 I = zeros(length(frequency),length(lensPointSourceDistance));
34 for p = 1:length(frequency)
35
36 for k = 1:length(lensPointSourceDistance)
37     elementPressure = zeros(length(elementnumber),1);
38
39     for i = 1:totalElements
40         pressure = zeros(length(yi), length(xi));
41
42         for m = 1:length(xi)
43             for n = 1:length(yi)
44
45                 pressure(n,m) = ...
                    peak_pressure(a,b,wavelength(p),lensTransducerDistance,...
                    lensPointSourceDistance(k),focalLength,xi(m),yi(n),mu,Δ0,...
                    pitch,totalElements,elementnumber(i),centering,y0);
46
47
```

```

48
49     end
50     end
51
52     elementPressure(i) = mean(mean(pressure));
53
54     end
55 I(p,k) = sum(abs(elementPressure));
56 end
57 p %this is to indicate how many frequencies have been evaluated, it can ...
    be removed
58 end
59
60 if length(frequency) ≥ 2
61     Int = sum(I);
62 else
63     Int = I;
64 end
65
66 ipValuesNorm = (ipValues./max(ipValues)).';
67 IntNorm = Int./max(Int);
68
69 figure
70 plot(ipAbsDepths, IntNorm)
71 hold on
72 plot(ipAbsDepths, ipValuesNorm, 'o')
73 xlabel('Depth [mm]')
74 ylabel('Pressure [a.u.]')
75 legend('Model', 'Experiment')

```

A.2 Peak pressure function

Below is the peak pressure function presented that is used in the main code. This function calculates the solution to equation (24).

```

1 function pressure = peak_pressure(a,b,wavelength,lensTransducerDistance,...
2     lensPointSourceDistance,focalLength,xi,yi,mu,delta0,...
3     pitch,totalElements,elementnumber,centering,y0)
4
5     L = (1./lensTransducerDistance - 1./focalLength + ...
6         1./lensPointSourceDistance);
7
8     x0 = (centering-elementnumber).*pitch; % Calculate the ...
9         displacement in x direction relative to center of the lens
10
11     % Calculate the integrals
12     intx = @(x) exp(i.*x.*(pi/wavelength).*(L.*x - ...
13         2.*(xi./lensTransducerDistance + x0./lensPointSourceDistance)));
14     inty = @(y) exp(i.*y.*(pi/wavelength).*(L.*y - ...
15         2.*(yi./lensTransducerDistance + y0./lensPointSourceDistance)));
16
17     integralx = integral(intx,-(1/2)*a,(1/2)*a,'AbsTol',1e-12');
18     integraly = integral(inty,-(1/2)*b,(1/2)*b,'AbsTol',1e-12');
19
20     % Multiply the solution to the integrals with the prefactors
21     pressure = (1./(lensTransducerDistance.*lensPointSourceDistance)).*...
22     exp(i.*(2*pi/wavelength).*(lensTransducerDistance + ...
23     lensPointSourceDistance + mu.*delta0)).*exp(i.*(pi/wavelength).*((xi.^2 ...
24     + yi.^2)/(lensTransducerDistance))).*exp(i.*...

```

```
19     (pi/wavelength).*((x0.^2 + ...  
20     y0.^2)/(lensPointSourceDistance)).*integralx.*integrally;
```